AGU PUBLICATIONS

JGR

Journal of Geophysical Research: Space Physics

RESEARCH ARTICLE
10.1002/2015JA021523

Ion upflow dependence on ionospheric density and solar photoionization

I. J. Cohen[1,2], M. R. Lessard[1], R. H. Varney[3], K. Oksavik[4,5], M. Zettergren[6], and K. A. Lynch[7]

[1]Space Science Center, University of New Hampshire, Durham, New Hampshire, USA, [2]Now at The Johns Hopkins University Applied Physics Laboratory, Laurel, Maryland, USA, [3]Center for Geospace Studies, SRI International, Menlo Park, California, USA, [4]Birkeland Centre for Space Science, Department of Physics and Technology, University of Bergen, Bergen, Norway, [5]Department of Arctic Geophysics, University Centre in Svalbard, Longyearbyen, Norway, [6]Department of Physical Sciences, Embry-Riddle Aeronautical University, Daytona Beach, Florida, USA, [7]Department of Physics and Astronomy, Dartmouth College, Hanover, New Hampshire, USA

Key Points:
- Simulations show that ionospheric density affects several aspects of ion upflow
- EISCAT radar observations support new simulation predictions of ionospheric density on ion upflow
- EISCAT observations show the seasonal variation in ionospheric density due to solar photoionization

Correspondence to:
I. J. Cohen,
ian.cohen@jhuapl.edu

Citation:
Cohen, I. J., M. R. Lessard, R. H. Varney, K. Oksavik, M. Zettergren, and K. A. Lynch (2015), Ion upflow dependence on ionospheric density and solar photoionization, *J. Geophys. Res. Space Physics*, *120*, 10,039–10,052, doi:10.1002/2015JA021523.

Received 3 JUN 2015
Accepted 21 OCT 2015
Accepted article online 17 NOV 2015
Published online 21 NOV 2015

Abstract Motivated by rocket observations showing a variety of different ionospheric responses to precipitation, this paper explores the influence of the background ionospheric density on upflow resulting from auroral precipitation. Simulations of upflow driven by auroral precipitation were conducted using a version of the Varney et al. (2014) model driven by precipitation characterized by observations made during the 2012 Magnetosphere-Ionosphere Coupling in the Alfvén resonator rocket mission and using a variety of different initial electron density profiles. The simulation results show that increased initial density before the onset of precipitation leads to smaller electron temperature increases, longer ionospheric heating timescales, weaker ambipolar electric fields, lower upflow speeds, and longer upflow timescales but larger upflow fluxes. The upflow flux can increase even when the ambipolar electric field strength decreases due to the larger number of ions that are accelerated. Long-term observations from the European Incoherent Scatter (EISCAT) Svalbard radar taken during the International Polar Year support the effects seen in the simulations. This correlation between ionospheric density and ion upflows emphasizes the important role of photoionization from solar ultraviolet radiation, which the EISCAT observations show can increase ionospheric density by as much as an order of magnitude during the summer months.

1. Introduction

It is now commonly understood that the ionosphere and magnetosphere are intimately coupled through the passage of currents and convection of plasma. Of particular importance to the magnetosphere-ionosphere system is the outflow of ionospheric plasma into the magnetosphere. Although it was originally believed that heavy ionospheric plasma could not achieve enough energy to escape the planet's gravitational pull, satellite observations soon showed evidence of significant quantities of such ionospheric plasma in the near-Earth environment [*Hoffman*, 1970; *Brinton et al.*, 1971; *Shelley et al.*, 1972].

This global outflow of plasma occurs through different processes at high latitude and midlatitude. In the polar cap, plasma is liberated through the classical polar wind, a thermal process by which light ions (H^+ and He^+) are carried out of the ionosphere along open field lines [*Banks and Holzer*, 1969]. This mechanism can also be affected by nonclassical processes in the polar cap involving photoelectrons, cusp electrons, wave-particle interactions, and the polar rain [*Schunk and Sojka*, 1997]. With the exception of H^+, the ions liberated by outflow processes require a secondary energization source to achieve escape velocity. This creates the distinction between ion upflow processes, which initially move ions to higher altitudes, and ion outflow processes that provide sufficient energy for the ions to escape Earth's gravity. Of particular note in this paper is the response of thermal upflowing ions (TUI). *Wahlund et al.* [1992] first separated TUI into two types: thermal plasma upflows (Type 1) and upflow due to enhanced field-aligned electric fields (Type 2). *Strangeway et al.* [2005] later built upon this classification, differentiating the types by energy transport: electromagnetic for Type 1 and particle for Type 2. New results show that upflowing/backscattered secondary electrons can also augment the self-consistent ambipolar electric field and contribute to ion upflow in the same way that photoelectrons do (A. Glocer, private communication, 2015).

Several statistical studies have specifically looked at the seasonal [*Yau et al.*, 1985; *Keating et al.*, 1990; *Foster*, 1997; *Ogawa et al.*, 2011] and solar cycle [*Ogawa et al.*, 2010] dependence of ion upflows. Of particular interest

Table 1. Table Showing the Variation in Observations of Electron Temperature and Densities Obtained During Rocket Missions at Different Altitudes on the Nightside and Dayside[a]

Rocket	Launch Site	Date (Time)	Apogee	T_e at Apogee (K)	n_e at Apogee (m^{-3})
MICA	Poker Flat, AK (nightside)	19 Feb 2012 (05:41 UT)	325 km	2200	1×10^{11}
Cascades-2	Poker Flat, AK (nightside)	20 Mar 2009 (11:04 UT)	564 km	1800	n/a
ACES High	Poker Flat, AK (nightside)	29 Jan 2009 (09:51 UT)	360 km	2600	7.4×10^{9}
SCIFER-2	Andøya, Norway (dayside)	18 Jan 2008 (07:30 UT)	1468 km	3200	n/a
SERSIO	Ny-Alesund, Norway (dayside)	22 Jan 2004 (08:57 UT)	762 km	6700	5.5×10^{10} (radar)

[a]Density measurements presented for SERSIO were obtained by the EISCAT Svalbard radar [*Frederick-Frost et al.*, 2007].

is the work of *Yau et al.* [1985], who presented satellite observations of increased O^+ upflow occurrence during the summer and suggested a connection to solar EUV flux. *Ogawa et al.* [2011] also showed an increase in upflow flux during summer months but a simultaneous decrease in upflow occurrence. *Ogawa et al.* [2010] found similar trends when looking at the solar cycle dependence of ion upflow. During solar maximum, they showed evidence of decreased upflow velocities, increased upflow fluxes, and decreased upflow occurrence.

Observations from rocket missions on both the dayside and nightside have found evidence of varying electron temperature and density (as summarized in Table 1). These contrasting measurements associated with soft or more energetic precipitation and observed at different altitudes motivate questions regarding the relationship between electron temperatures and densities and, ultimately, the role these ionospheric parameters might play in ion upflow. In particular, this study focuses on Type-2 upflow initiated by the precipitation of soft electrons, which can deposit a significant amount of energy into the auroral ionosphere. This energy deposition can have many effects on the ionosphere and subsequently on the magnetosphere-ionosphere system. For example, *Strangeway et al.* [2005] and many other authors have concluded that the establishment of a vertical ambipolar field by the deposition of energy from soft electron precipitation is a significant driver of Type-2 ion upflow. Simply, precipitating electrons collisionally heat ionospheric electrons and create electron pressure gradients that establish the field-aligned ambipolar electric field, which accelerates ions and generates upflow. These pressure gradients can be further augmented by suprathermal electron populations [*Khazanov et al.*, 1997, 1998; *Glocer et al.*, 2012; *Varney et al.*, 2014]. Likewise, *Clemmons et al.* [2008] and *Zhang et al.* [2012] proposed processes by which soft electron precipitation may play a role in heating neutrals and contribute to neutral upwelling. In both cases, precipitation can lead to important ionospheric dynamics affecting both magnetospheric and ionospheric regions and processes.

Of particular interest in Table 1 is the order of magnitude variation in electron density measurements made by Magnetosphere-Ionosphere Coupling in the Alfvén resonator (MICA) and Auroral Current and Electrodynamics Structure (ACES) High. These missions had similar apogees and auroral characteristic energies, which would lead one to expect similar ionospheric response and resulting parameters. The higher temperatures seen at elevated altitudes by Sounding of the Cleft Ion Fountain Energization Region-2 (SCIFER-2) and Svalbard EISCAT Rocket Study of Ion Outflows (SERSIO) are most likely due to softer (lower energetic) dayside precipitating electrons that do not penetrate as deeply into the ionosphere and therefore deposit energy at higher altitudes. These varying observations of electron temperature and density from the dayside and nightside at different altitudes make it difficult to develop a cohesive understanding of the dynamics of ionospheric response to auroral precipitation and the role they might play in processes such as ion outflow.

These rocket observations, particularly on the nightside, are critical and unique measurements of ionospheric parameters at the ionospheric footprint of the Earth's magnetic field lines. As such, the obvious variation in observations led to questions about how conditions near the ionospheric field line footprint might impact and relate to ion upflow dynamics at higher altitudes. This paper presents a one-dimensional ionospheric simulation based on the model by *Varney et al.* [2014] to investigate the potential impact that these varying low-altitude parameters might have on upflow dynamics at higher altitudes along the field line. Section 2 describes the model and section 3 presents the model results. Discussion and conclusions are found in sections 4 and 5, respectively.

2. Model Description

The single field line ionosphere/polar wind model introduced by *Varney et al.* [2014] solves the dynamics of thermal ions, thermal electrons, and suprathermal electrons on a single field line between 97 and 6300 km altitude. The thermal ions use the eight-moment transport equations for H^+, He^+, and $O^+(^4S)$, and photochemistry only for N^+, NO^+, O_2^+, N_2^+, $O^+(^2D)$, and $O^+(^2P)$. In the eight-moment approximation the heat flow vector is treated at the same level as the density, velocity, and pressure. This inclusion captures the thermal diffusion effect (i.e., heat flow effects on the ion velocities through collisions) and the diffusion thermal effect (i.e., velocity effects on the heat flows through collisions). The eight-moment approximation does not include temperature anisotropy or any other higher order moments of the distribution function. As such, this approximation is not valid above 3000 km [*Robineau et al.*, 1996]. Tests with the model have demonstrated that the results below 2000 km are insensitive to the location of the upper boundary as it is moved between 3000 and 8000 km. Thus, this fluid model is still appropriate for investigations of the ionosphere below 2000 km. It should be noted that the model uses a thermosphere generated by NRLMSISE-00 [*Picone et al.*, 2002] and neutral upwelling effects are not included.

The thermal electrons are governed by quasineutrality, current continuity ($\nabla_{\parallel} \cdot \mathbf{J}_{\parallel} = 0$), and a time dependent electron energy equation that includes heating from suprathermal electrons, heat flows associated with thermal conduction, and the thermoelectric effect. A steady state linearized kinetic solver is used for the suprathermal electron population. This solver is a version of the photoelectron model introduced by *Varney et al.* [2012] with the addition of ambipolar electric field effects. The suprathermal electron solution is used to compute a thermal electron heating rate and ion production rates through impact ionization.

All of the plasma populations are connected through the self-consistent ambipolar electric field. As explained in the appendix of *Varney et al.* [2014], this field is computed in such a way that it implicitly includes the augmentation of the field by suprathermal electron effects. For the simulation runs shown here, the suprathermal energy grid has been extended up to 10 keV to allow for inclusion of more energetic precipitation than was originally considered by *Varney et al.* [2014]. For all of the simulations presented here, the suprathermal electron solver is recalled every 1 s as opposed to every 180 s as was done for the simulations presented by *Varney et al.* [2014].

The upper boundary of the model uses Neumann boundary conditions for the ions and upflowing suprathermal electrons, thus allowing outflow through the top of the model. These upper boundary conditions are appropriate for open field lines in all cases and for closed field lines in the case of discrete aurora. The parallel electric field that forms above a discrete auroral arc to accelerate electrons downward will also accelerate ions upward, thus preventing any ions from flowing back downward. The model runs require a specification of the downflowing suprathermal electron distribution (i.e., precipitation), an electron temperature gradient at the upper boundary, a potential difference between the upper boundary and infinity that may reflect suprathermal electrons back down, and a field-aligned current (FAC).

The simulations presented here intend to reproduce a discrete auroral arc. The precipitating distributions above discrete arcs are typically Maxwellian or Kappa distributions with characteristic energies of 600–1100 eV accelerated through field-aligned potential drops of 1–3 keV [see *Kaeppler et al.*, 2014, and references therein]. Any backscattered secondary electrons with energies less than the field-aligned potential drop will be trapped [*Chiu and Schulz*, 1978]. For these simulations presented below, we specify a field-aligned potential drop and the characteristic energy of an accelerated Maxwellian distribution. The potential drop is assumed to be immediately above the upper boundary of the model, which is comparable to the typical altitudes of parallel electric fields inferred from observations [*Bennett et al.*, 1983]. Following the procedure of *Varney et al.* [2014] to simulate electron trapping by a potential drop, the distribution of downward electrons at energies below the energy of the potential drop is a copy of the upward distribution. When a potential drop exists, thermal electrons may neither inflow nor outflow across the potential drop. Thermal electrons on the ionospheric side will be trapped, and inflowing electrons from the magnetosphere will be accelerated through the potential drop and enter the ionosphere as suprathermal electrons. We set the thermal electron velocity to zero at the upper boundary and allow the FAC to be whatever it needs to be to make this happen. Furthermore, we set the thermal electron temperature gradient at the upper boundary to zero; the only energy flow from the magnetosphere is carried by the suprathermal electrons.

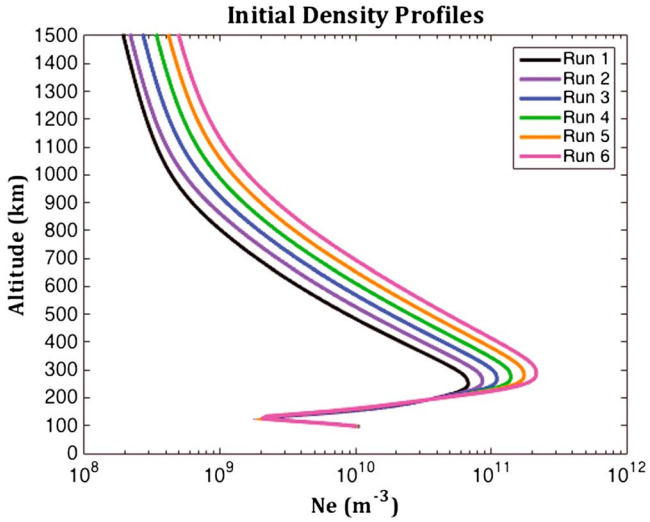

Figure 1. Initial ionospheric density profiles for the six nightside simulation runs.

In these simulations the high-energy backscattered secondaries that are not reflected by the potential drop are lost from the simulation. In reality these electrons follow closed field lines through the magnetosphere and could possibly come back to the ionosphere. Nonetheless, these electrons can be ignored because they are only ~5% of the precipitating flux. In diffuse aurora, however, no field-aligned potential drop exists and large fluxes of backscattered secondaries escape the ionosphere and impact the conjugate ionosphere, coupling the two hemispheres together [*Khazanov et al.*, 2014]. These processes require modeling the entire closed field line and are outside the scope of the current study.

3. Model Results

The simulations presented below are 1080 s short runs starting from 05:48 UT on 19 February 2012 where precipitation is turned on for the first 360 s. In order to obtain initial conditions for these short runs, the model was run for 48 h prior to the start time of the short runs with no precipitation. The short runs are initialized using the complete internal model state at the end of the long runs. At the end of these long runs the model has settled into a slowly varying, quasi-equilibrium; the transients observed in the short runs are entirely due to the introduction of precipitation and not to the choice of initial conditions. In order to create initial conditions with a variety of background densities, the six different long runs were performed using six different $F_{10.7}$ values ranging from 70 to 120 in the solar EUV model. Figure 1 shows the electron density profiles from the end of these six long runs. On the days prior to the MICA launch, $F_{10.7}$ was approximately 100, and the long run using a $F_{10.7}$ of 100 produces a peak F region electron density of 1.40×10^{11} m^{-3}, which is close to the actual Poker Flat Incoherent Scatter Radar observations from that night.

Unfortunately, the energetic electron instrument on MICA experienced a malfunction; however, the precipitating electron characteristics were estimated by a new method that combines the determination of energy flux from all-sky observations of 427.8 nm emission with characteristic energies ascertained from scanning Doppler imaging measurements (Hampton et al., Detailed regional auroral electron energy deposition estimations using measurements of E region temperature and N_2^+ first-negative emissions: A MICA case study, *Journal of Geophysical Research: Space Physics*, in preparation). The optical data indicate an average energy of 3450 eV and a number flux of 2.6×10^{12} m^{-2} s^{-1} mapped to 6300 km. However, the optical data cannot determine what portion of the energy comes from the high-altitude potential drop. Following typical numbers from *Kaeppler et al.* [2014], we assume the unaccelerated electrons have a Maxwellian distribution with a characteristic energy of 800 eV (1600 eV average energy), and that the remaining 1850 eV come from the parallel potential drop. Additional experiments (not shown) confirm negligible variation (3%) in the temperature profiles as the characteristic energies are varied between 600 and 1100 eV, so long as the total average energy after the potential drop remains constant. Figure 2 shows altitude profiles for the rates of electron heating and total impact ionization resulting from the precipitation in the simulations. Note that the heating rates

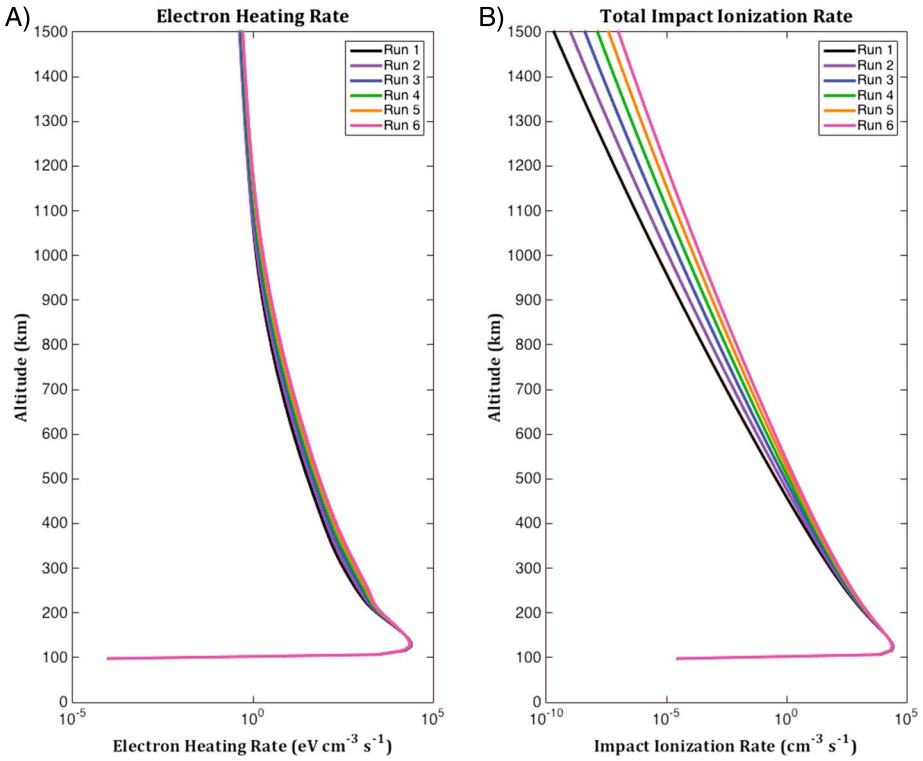

Figure 2. Altitude profiles for the rates of (a) electron heating and (b) total impact ionization for each of the six simulation runs.

decrease along with the electron densities as the portion of energy lost to thermal electrons versus neutral particles follows the ratio of n_e/n_n.

Since the simulations showed upflow in response to auroral precipitation (as observed by the MICA mission), this study focuses solely on Type-2 upflow dynamics. It should be emphasized that the model is able to generate realistic upflows for the MICA event (compared with typical upflow values seen by the European Incoherent Scatter (EISCAT) radar, to be discussed in section 4.1) without needing to consider additional physics, such as contributions from parallel electric fields associated with anomalous resistivity related to

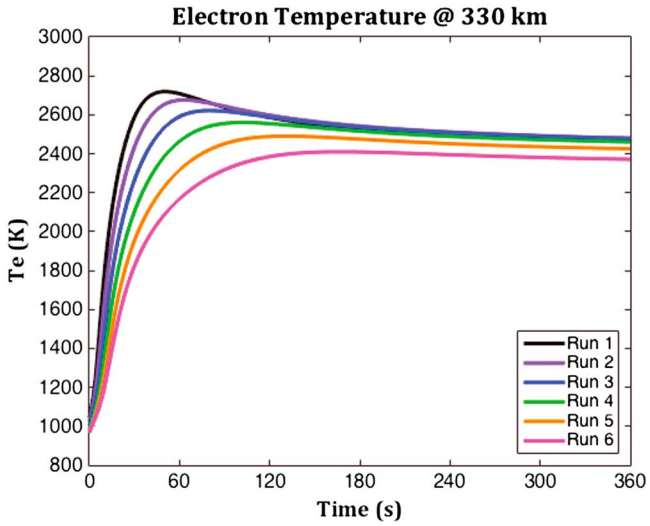

Figure 3. Comparison of the evolution of electron temperature at 330 km for the six simulation runs during active precipitation. The color of each line corresponds to the initial density profile of that simulation, as shown in Figure 1.

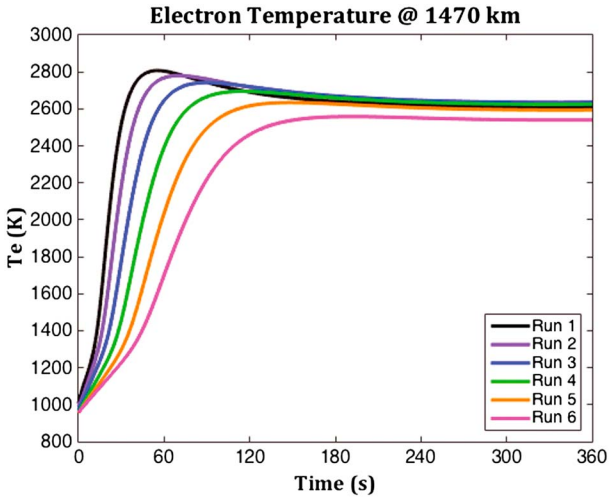

Figure 4. Comparison of the evolution of electron temperature at 1470 km for the six simulation runs during active precipitation. The color of each line corresponds to the initial density profile of that simulation, as shown in Figure 1.

turbulence [*Kagan and St. Maurice*, 2005]. Other papers from the MICA mission focus on hysteresis in the *F* region densities [*Zettergren et al.*, 2014] and current closure [*Lynch et al.*, 2014].

To ensure that the results were reasonable, the electron temperature at 300 km in the simulations was compared with the observations from MICA. As shown in Figure 3, the simulation generated the enhanced electron temperatures associated with Type-2 upflows [*Wahlund et al.*, 1992], with temperatures ranging from approximately 1000 to 2700 K during the precipitation. The temperatures in the simulations tended to settle to equilibrium around 2400–2500 K, slightly higher than the 2200 K seen by MICA at apogee. This is most likely due to an overestimation of the precipitating flux resulting from failure to account for extra blue line emission generated by trapped secondaries when fitting the optical data. However, Figure 3 clearly shows that larger densities limit the peak electron temperature; this inverse relationship between electron density and temperature agrees with observations by *Brace and Theis* [1978].

Although the MICA mission did not obtain in situ observations above 326 km, simulation results of the thermal evolution at very high altitudes (Figure 4) were also considered. Comparison of Figures 3 and 4 shows that the simulation did not result in much variation in temperature between very high and *F* region altitudes. Overall, these temperatures are much lower than those measured by the dayside rockets. This is most likely attributable to the more energetic precipitation of the MICA event, which penetrates to lower altitudes. However, Figure 4 does show that the time required to reach the peak temperature for each run increases with density. In other words, higher electron density means the fixed input energy is spread over more particles, resulting in less energy per particle and lower temperature. These lower temperatures mean lower thermal conductivity, which results in a longer "cooking time" for the heat to propagate to the higher altitudes. SCIFER-2 observed spikes in electron temperature at very high altitudes (>1400 km) on the dayside, and *Lund et al.* [2012] were able to determine that a ~100 s "cooking time" was required to reach those elevated temperatures after the onset of precipitation. The simulation results in Figure 4 show "cooking times" to reach maximum temperature that range from approximately 60–120 s, which are of the order of 100 s and consistent with the observations from SCIFER-2.

Because of its importance in the generation of Type-2 upflow, the effect of density variations on the ambipolar electric field was studied as well. Figure 5 shows the evolution of the ambipolar electric field (E_a) versus altitude during the 360 s of precipitation for each of the six simulation runs. Notice how the ambipolar field weakens as the background density increases. This seems reasonable since increased electron density will result in reduced electron temperature, which contributes to the ambipolar diffusion that generates the field-aligned ambipolar electric field. Given this result and the ambipolar field's role in driving Type-2 upflow one would expect that increased density would inhibit upflow in the simulations. As expected, Figure 6 shows that the upflow velocity decreases as the density increases. However, despite the weakened ambipolar field and decreased upflow speeds, the overall upflow fluxes shown in Figure 7 increase with density. Here the O^+ number flux ($n_O^+ v_O^+$) is plotted versus altitude at 1 min intervals during the 360 s of precipitation for each of the runs.

Several effects are immediately evident from these results. First, there is an obvious change in upflow behavior above and below the *F* region peak (approximately 275 km, as shown in Figure 1). Notice that this is approximately the same altitude above which the bulk of the ambipolar field is established, as shown in Figure 5. It is approximately at the *F* region peak where ionospheric dynamics switch from being chemistry dominated

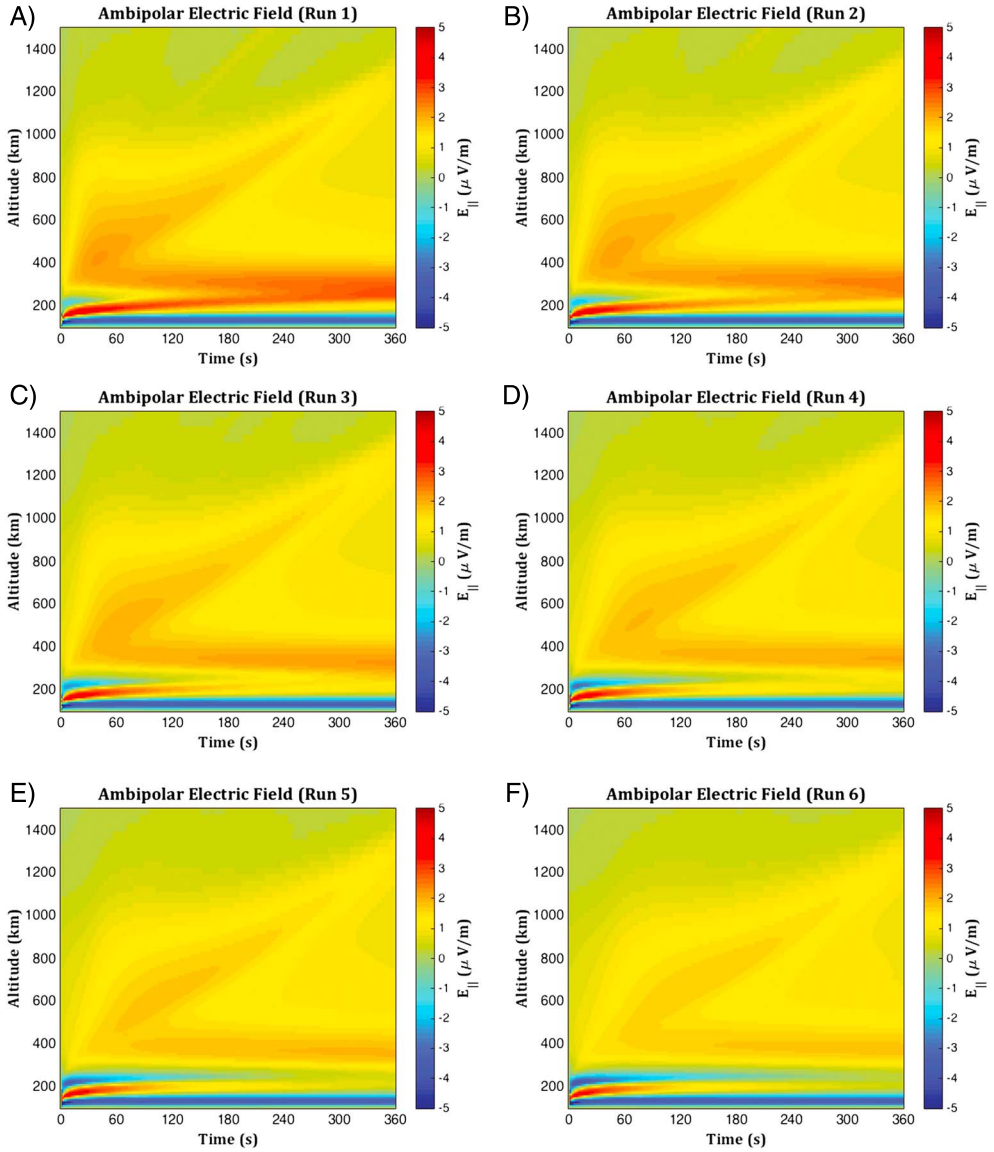

Figure 5. The strength of the ambipolar electric field (E_a) versus altitude during the 360 s of precipitation for each of the six simulation runs.

(below) to being transport dominated (above). At altitudes below the *F* region peak, the plasma attempts to respond to the energy deposited by the precipitation via transport, but this response is overshadowed by chemistry effects. For this reason, this study will focus on the effects at *F* region and topside altitudes above roughly 350 km, where appreciable upflow is shown to result from the precipitation. Second, at these higher altitudes the runs with increased densities show more significant upflow. Finally, notice that upflow in the lower density runs starts to move to higher altitudes faster than the higher density runs. This is understandable due to the longer heating timescales and slower upflow velocities seen at higher densities.

4. Discussion

The simulation results indicate that at these *F* region and topside altitudes, increased density results in increased upflow of O^+. It seems counterintuitive that enhanced ionospheric density would correlate with increased upflow since Figure 5 shows that an increase in density decreases the strength of the ambipolar field. However, the momentum equation for the dominant ion species can be expressed as

$$\frac{\partial}{\partial t}(m_i n_i v_i) + \nabla \cdot (m_i n_i v_i v_i) = -\nabla(k_B n_i T_i) + n_i e E_a + \frac{\delta M}{\delta t}, \quad (1)$$

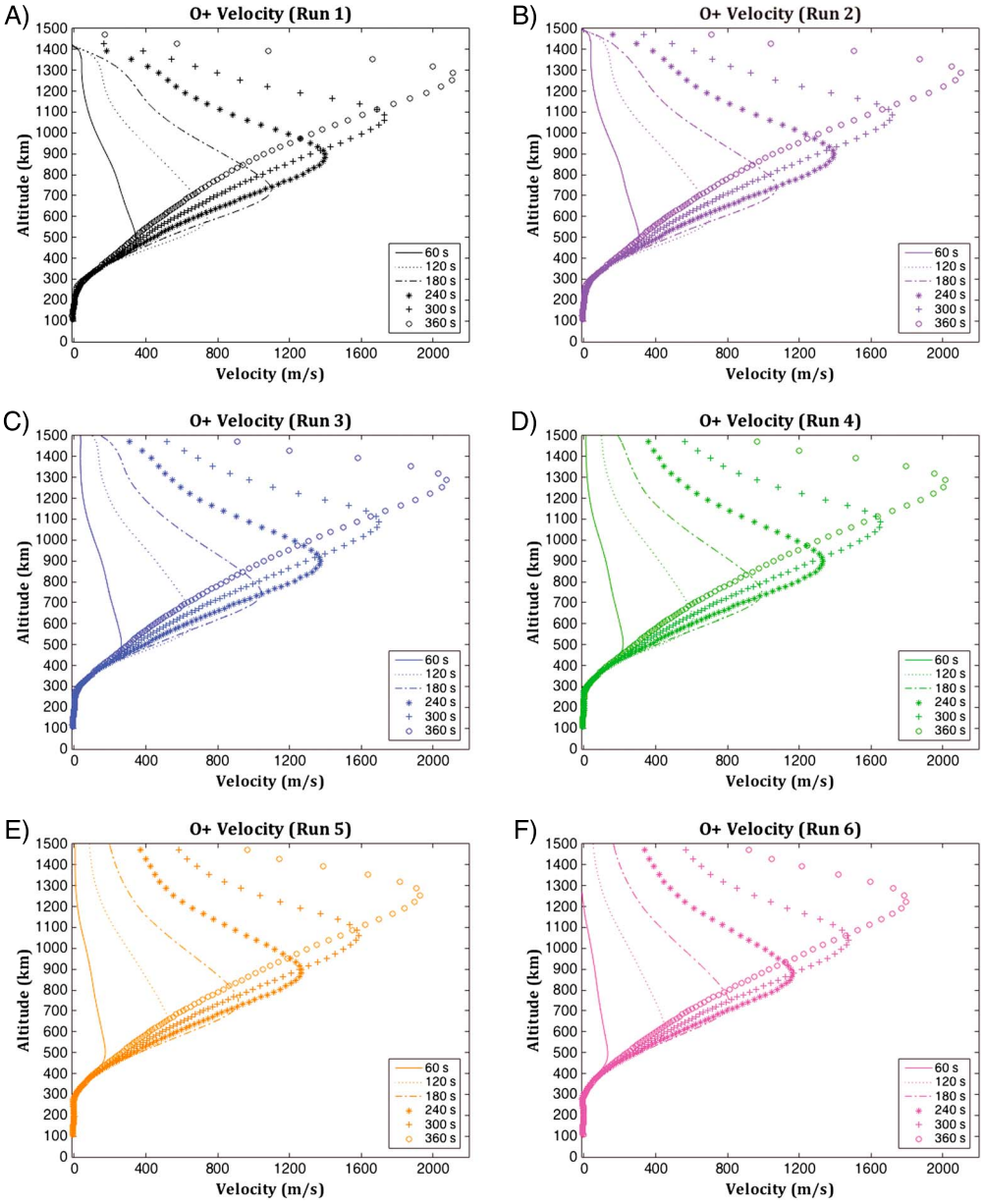

Figure 6. Comparison of the evolution of O^+ upflow velocity (v_O^+) at 1 min intervals during the phase of active precipitation across the six simulation runs. The colors correspond to colors of the initial density profiles for each run, as shown in Figure 1.

where m_i, n_i, and v_i are the ion mass, density, and velocity, respectively; n_i and T_i are the ion density and temperature, respectively; k_B is the Boltzmann constant; e is the elementary charge; E_a is the ambipolar electric field; and $\delta M/\delta t$ includes the remaining collisional terms. All of the terms in the momentum equation are proportional to the ion density, so it is not surprising that density variation has a noticeable effect on the ionospheric dynamics. The ambipolar electric field can be expressed as

$$E_a = \frac{-1}{en_e}\nabla(k_B n_e T_e) = \frac{-k_B}{e}\left[\nabla T_e + T_e\frac{\nabla n_e}{n_e}\right]. \quad (2)$$

At high altitudes ∇T_e is small, so the $T_e\nabla \ln(n)$ term dominates. While smaller T_e is associated with smaller E_a, the decrease in T_e is slower than $1/n$, so the quantity nE_a seen in equation (1) actually increases with density even though T_e and E_a decrease.

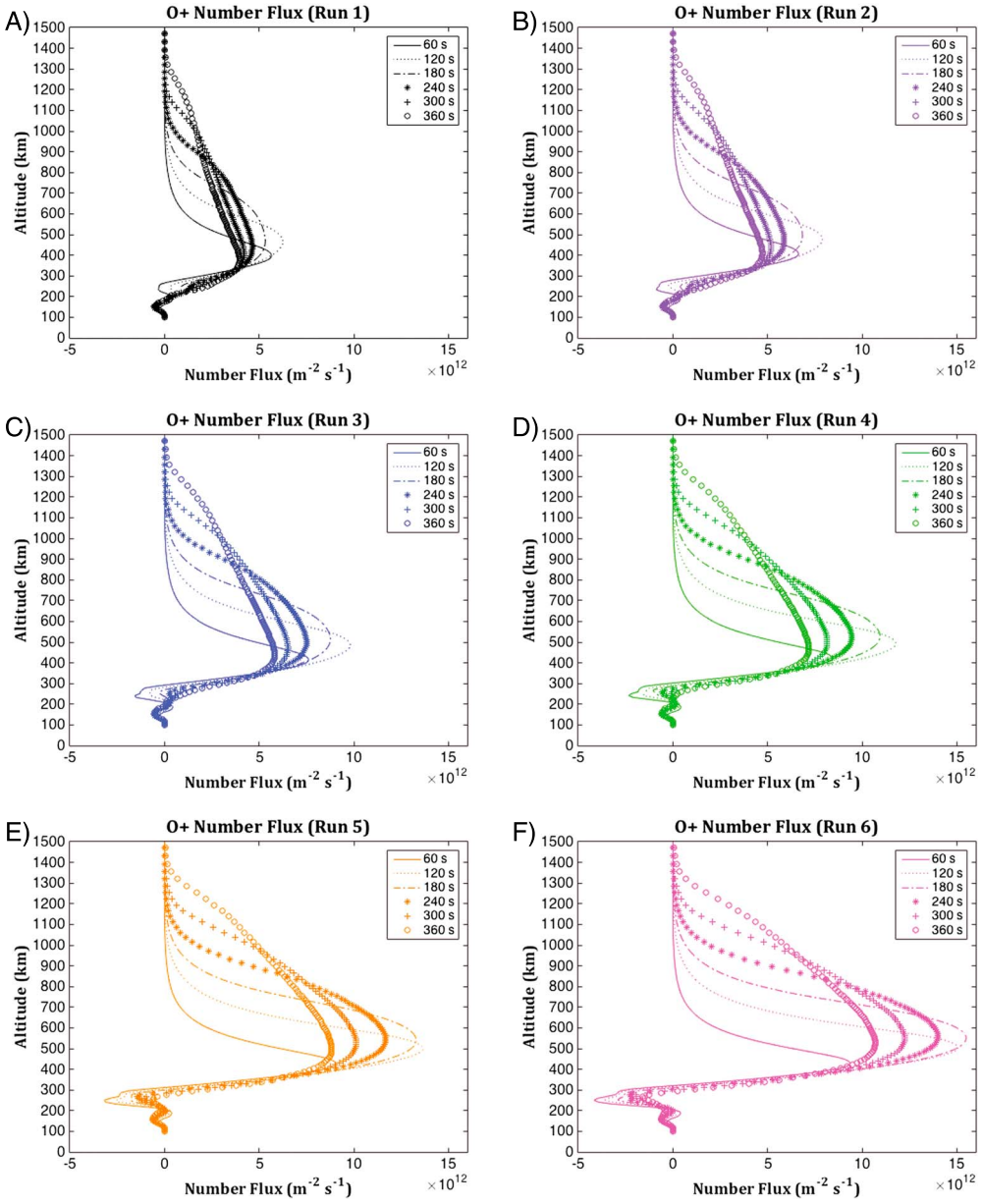

Figure 7. Comparison of the evolution of O^+ number flux ($n_O^+ v_O^+$) at 1 min intervals during the phase of active precipitation across the six simulation runs. The colors correspond to colors of the initial density profiles for each run, as shown in Figure 1.

To summarize, enhanced ionospheric plasma density in the model results in (i) lower ionospheric electron temperatures, (ii) longer ionospheric heating timescales, (iii) weaker ambipolar electric fields, (iv) lower O^+ upflow speeds, (v) longer upflow timescales, and (vi) larger net O^+ upflow fluxes.

4.1. The Role of Solar Photoionization

Of the many natural effects that can affect ionospheric density, the most significant is solar photoionization [e.g., *Moen et al.*, 2008]. Figure 8 elucidates the seasonal ionospheric density variation caused by solar photoionization. It shows data from the 42 m EISCAT Svalbard radar taken during the International Polar Year (IPY), which spanned parts of 2007 and 2008 [*Ogawa et al.*, 2011]. Figure 9 presents observational evidence of the role of solar photoionization on ionospheric density and its effect on ion upflows. Figure 9a shows the estimated lowest illuminated altitude (or altitude of the terminator) over the EISCAT Svalbard radar at 09:00 UT

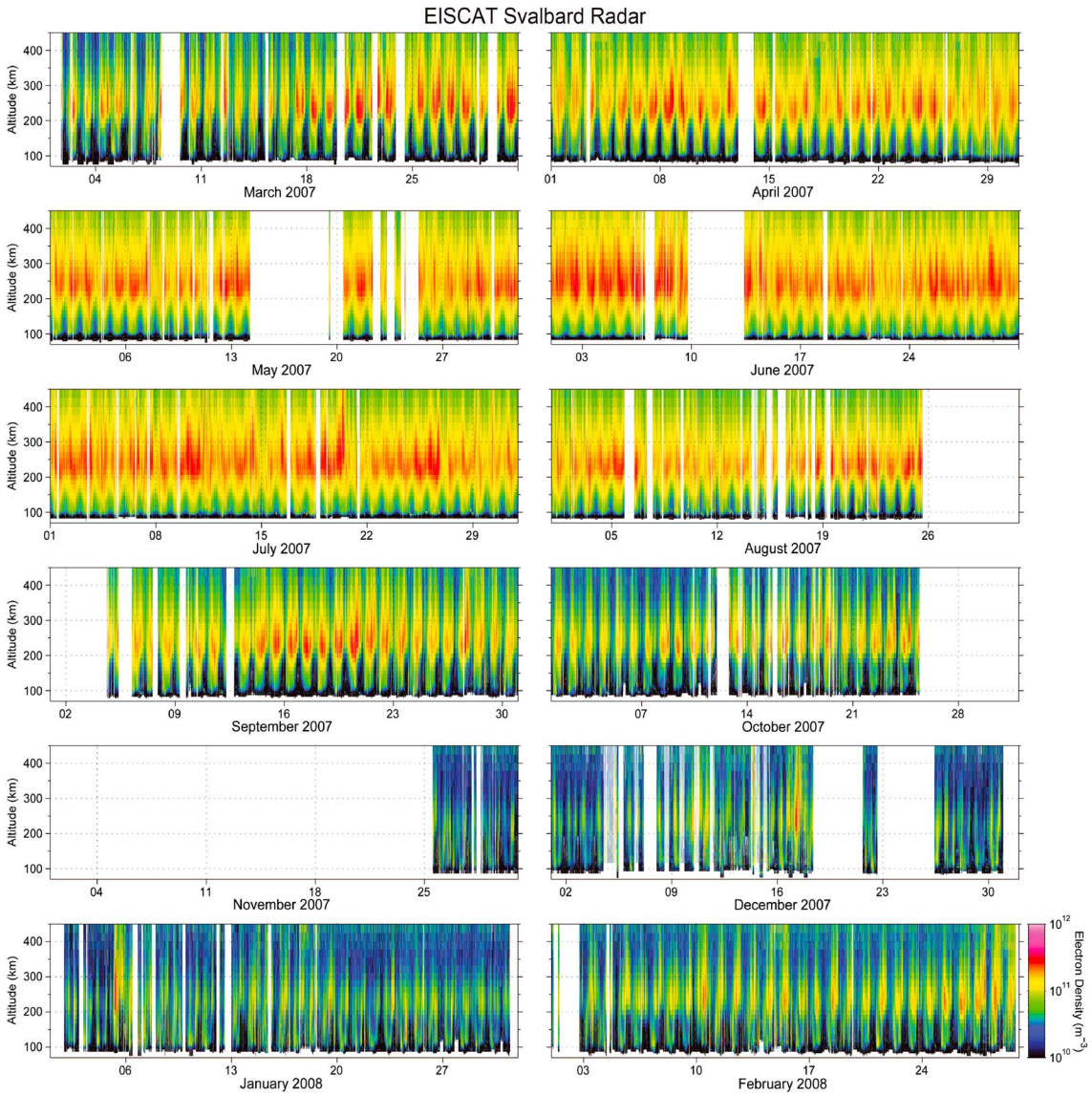

Figure 8. Data from the 42 m EISCAT Svalbard radar taken during the International Polar Year (IPY) clearly showing the seasonal effect of solar photoionization on ionospheric density.

for each day from March 2007 through February 2008, the same time period shown in Figure 8. These altitudes were calculated using the solar zenith angle, a spherical Earth, and the fact that in the midst of winter the sunlight will reach to some lowest global illuminated altitude h_{min} somewhere at lower latitudes south of the EISCAT radar. The colored lines indicate calculations made for different estimations of h_{min}, which generally agree with the model results of *Lorentzen et al.* [2010]. The left axis in Figure 9a shows the altitude along the EISCAT Svalbard Radar beam, and the color scale is the minimum height that a ray of sunlight has reached prior to entering the EISCAT beam. For March to November, the parameter h_{min} is identical to the altitude, meaning that the sunlight enters the EISCAT beam from above. For November to February, h_{min} is less than the altitude, meaning that the sunlight enters the EISCAT beam from below. Let us take 300 km altitude as an example. From March to November, the color in 300 km altitude is yellow (h_{min} = 300 km); i.e., the sunlight creating ionization in the EISCAT beam in 300 km altitude has never been below 300 km altitude and is still fully potent to create ionization. For 21 December, the color in 300 km altitude is between bright and dark blue (h_{min} = 150 km); i.e., the sunlight creating ionization in 300 km altitude on 21 December has intersected the lower latitude atmosphere at 150 km altitude before it intersects the EISCAT radar beam in 300 km altitude. This sunlight is far less capable of creating ionization in the EISCAT beam, and hence, there is significantly less

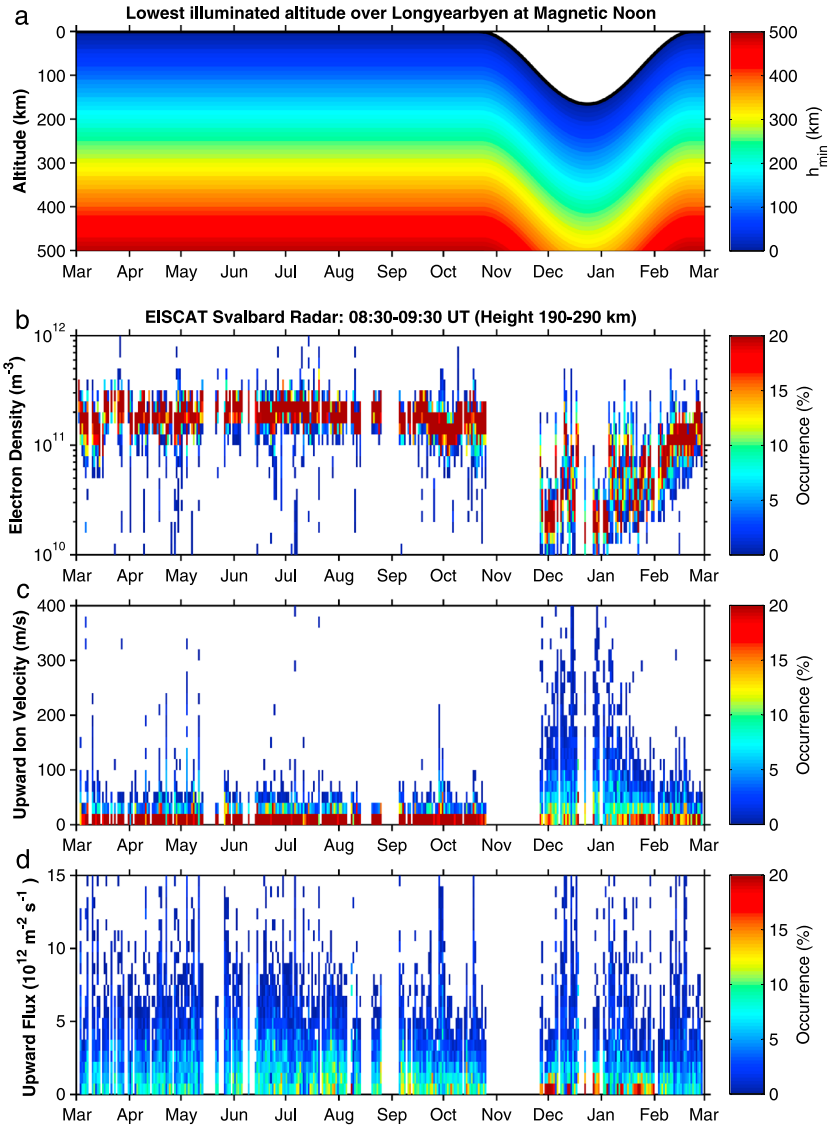

Figure 9. (a) The estimated lowest illuminated altitude (or altitude of the terminator) over the EISCAT Svalbard radar at 09:00 UT for each day from March 2007 to February 2008, the same time period shown in Figure 8. The colors represent calculations made for different values of the lowest global illuminated altitude (h_{min}). (b–d) The electron density, upward ion velocity, and upward ion flux values observed each day by the 42 m EISCAT Svalbard radar from 08:30 to 09:30 UT between 190 and 290 km. Note that the radar data show lower upflow velocities and higher fluxes in the summer months when electron density is enhanced.

ionization in winter months although the ionosphere is still "sunlit." We present the color scale to emphasize that the whole vertical column is affected (0 to 500 km altitude), and that the spectrum is less potent when it enters the EISCAT beam (due to the low height (h_{min}) that the sunlight has been at prior to entering the EISCAT beam in the midst of winter). The plateau seen from March through October indicates that the maximum illuminated latitude and location of h_{min} is at or poleward (north) of the EISCAT radar. Conversely, the maximum illuminated latitude and location of h_{min} is equatorward (south) of EISCAT during the winter (November through February), resulting in far less ionization by solar EUV in the EISCAT Svalbard Radar beam as the terminator moves up in altitude along the flux tube. Figures 9b–9d show the electron density, upward ion velocity, and upward ion flux, respectively, seen by EISCAT between 08:30 and 09:30 UT each day from March 2007 through February 2008. Note that the increased electron densities seen during the summer months correlate with decreased upflow velocities and increased fluxes comparable to the simulation results presented in Figures 6 and 7.

None of the aforementioned statistical studies of upflow have highlighted the impact of electron density. Our simulation results agree very well with the observations of *Yau et al.* [1985] but seem to disagree with *Ogawa et al.* [2011], who showed a decrease in upflow occurrence. However, this decrease might be due to limitations in their definition of an upflow event. To allow for identification of an upflow event in their EISCAT data, they required an upflow velocity of 100 m/s at three or more consecutive heights along the radar profile. However, Figure 6 clearly shows that increased density can reduce the upflow velocity, which may have led to less upflows reaching the velocities necessary to be considered as an event in their analysis. This identification method might also explain the opposing temperature and upflow correlations between our results and the observations of *Ogawa et al.* [2003, 2008, 2010]. Since increased ionospheric density results in both decreased upflow velocity and decreased electron temperature, the nonclassification of upflow events with lower upflow speeds would systematically exclude the events with lower electron temperatures.

Furthermore, the simulation results help give some context for the results of *Ogawa et al.* [2010]. Knowing that elevated ionospheric density affects upflows, it is not surprising that the solar cycle dependence of upflows parallels the seasonal variation since enhanced solar activity also increases ionospheric density [e.g., *Mechtly et al.*, 1972; *Zhang and Holt*, 2004; *Bilitza et al.*, 2007]. *Wang and Luhr* [2013] focused on auroral latitudes using data from the Defense Meteorological Satellite Program (DMSP) satellites and showed increased ion fluxes during the darker winter months, which disagrees with the conclusion that increased ionospheric densities lead to increased upward ion flux. However, it must be underscored that *Wang and Luhr* [2013] only looked at Type-1 upflow events associated with subauroral polarization streams (SAPs).

5. Conclusions

Understanding the ionospheric response to auroral precipitation is a key to understanding the very fundamentals of magnetosphere-ionosphere coupling. Rocket measurements of ionospheric parameters such as electron density and temperature vary significantly and motivate new questions regarding the effect of conditions at the ionospheric footprint of magnetic field lines on magnetospheric dynamics at higher altitudes. In particular, this study investigated the potential correlations between electron temperature and density and ion upflow. To do this, a one-dimensional ionospheric simulation based on the model by *Varney et al.* [2014] was run with precipitation characterized by ground-based observations made during the MICA sounding rocket mission. To understand the effects of ionospheric density on upflow, six simulations were run with ionospheric density profiles peaking from 6.8×10^{10} to 2.16×10^{11} m^{-3}.

The simulation results generated realistic ion upflows in response to the auroral precipitation and electron temperatures in good agreement with MICA observations at *F* region altitudes (300 km). The simulations also showed that electron density affects the timescales for high-altitude heating. In general, the simulations showed enhanced electron temperatures at very high altitudes within several minutes, which agrees well with observations by *Lund et al.* [2012]. Furthermore, the simulations demonstrated that increased density inhibits the strength of the ambipolar field that is established as a result of precipitation. However, the simulations also show that despite the weakened ambipolar field, upflow fluxes are still enhanced at higher densities because more ions are present to be influenced by the field. Moreover, at higher densities the associated upflow timescales are increased and upflow velocities are inhibited.

The simulations presented here generate the enhanced electron temperatures often associated with Type-2 upflows [*Wahlund et al.*, 1992] and exhibit the inverse relationship between the density and temperature, which agrees with observations by *Brace and Theis* [1978]. While the correlation between increased density and increased upflow fluxes suggested by our simulations might seem inconsistent with other studies that have established the correlation between increased temperature and increased upflows [*Skjæveland et al.*, 2014], the simulations strongly imply that the temperature increase in response to a fixed amount of precipitation will be less when the density is higher. Furthermore, the simulation results presented here show that photoionization of flux tubes by sunlight can have a large effect on upflows as it can increase ionospheric densities by as much as an order of magnitude seasonally. New EISCAT data from the International Polar Year (IPY) underscores this effect, clearly showing the seasonal effect of solar UV ionization on ionospheric density.

Acknowledgments
The rocket data presented here were collected by missions supported by the staff and engineers at NASA Wallops Flight Facility; additional rocket data may be obtained from Marc Lessard (email: marc.lessard@unh.edu). The model source code, output data, and analysis routines used in this paper will be preserved on a long-term storage system. These items will be made available upon request to R.H. Varney (email: roger.varney@sri.com). The EISCAT data are available from http://eiscat.se/. EISCAT is an international association supported by research organizations in China (CRIRP), Finland (SA), Japan (NIPR and STEL), Norway (NFR), Sweden (VR), and the United Kingdom (NERC). The authors thank the EISCAT staff and several volunteers for their outstanding efforts to keep the EISCAT Svalbard Radar running during the whole International Polar Year (IPY). Furthermore, the authors would like to thank Steve Kaeppler (SRI) for meaningful conversations that contributed to the development of this paper. Funding for this research at the University of New Hampshire was supported by NASA grants NNX10AL17G and NNX13AJ94G and AFOSR grant FA9550-14-1-0368. R.H. Varney is supported by the Dartmouth NASA Space Grant Visiting Young Scientist Program and NSF grant AGS-1555801. The work of K. Oksavik is supported by the Research Council of Norway under contracts 212014 and 223252. The EISCAT IPY data were covered by additional funding from Norway (NFR) and the project IPY-ICESTAR.

References

Banks, P. M., and T. E. Holzer (1969), High-latitude plasma transport: The polar wind, *J. Geophys. Res.*, *74*(26), 6317–6332.
Bennett, E. L., M. A. Temerin, and F. S. Mozer (1983), The distribution of auroral electrostatic shocks below 8000-km altitude, *J. Geophys. Res.*, *88*(A9), 7107–7120.
Bilitza, D., V. Truhlik, P. G. Richards, L. Triskova, and T. Abe (2007), Solar cycle variations of mid-latitude electron density and temperature: Satellite measurements and model calculations, *Adv. Space Res.*, *39*(5), 779–789.
Brace, L. H., and R. F. Theis (1978), An empirical model of the interrelationship of electron temperature and density in the daytime thermosphere at solar minimum, *Geophys. Res. Lett.*, *5*(4), 275–278.
Brinton, H. C., J. M. Grebowsky, and H. G. Mayr (1971), Altitude variation of ion composition in the midlatitude trough region: Evidence for upward plasma flow, *J. Geophys. Res.*, *76*(16), 3738–3745.
Chiu, Y. T., and M. Schulz (1978), Self-consistent particle and parallel electrostatic field distributions in the magnetospheric-ionospheric auroral region, *J. Geophys. Res.*, *83*(A2), 629–642.
Clemmons, J. H., J. H. Hecht, D. R. Salem, and D. J. Strickland (2008), Thermospheric density in the Earth's magnetic cusp as observed by the Streak mission, *Geophys. Res. Lett.*, *35*, L24103, doi:10.1029/2008GL035972.
Foster, C. (1997), Auroral ion upflows in the F-region and topside ionosphere, PhD thesis, Univ. of Leicester, Leicester, U. K.
Frederick-Frost, K. M., K. A. Lynch, P. M. Kintner, E. Klatt, D. Lorentzen, J. I. Moen, Y. Ogawa, and M. Widholm (2007), SERSIO: Svalbard EISCAT rocket study of ion outflows, *J. Geophys. Res.*, *112*, A08307, doi:10.1029/2006JA011942.
Glocer, A., N. Kitamura, G. Toth, and T. I. Gombosi (2012), Modeling solar zenith angle effects on the polar wind, *J. Geophys. Res.*, *117*, A04318, doi:10.1029/2011JA017136.
Hoffman, J. H. (1970), Studies of the composition of the ionosphere with a magnetic deflection mass spectrometer, *Int. J. Mass Spectrom. Ion Phys.*, *4*, 315–322.
Kaeppler, S. R., M. J. Nicolls, A. Strømme, C. A. Kletzing, and S. R. Bounds (2014), Observations in the E region ionosphere of kappa distribution functions associated with precipitating auroral electrons and discrete aurorae, *J. Geophys. Res. Space Physics*, *119*, 10,164–10,183, doi:10.1002/2014JA020356.
Kagan, L. M., and J.-P. St. Maurice (2005), Origin of type-2 thermal-ion upflows in the auroral ionosphere, *Ann. Geophys.*, *23*, 13–24.
Keating, J. G., F. J. Mulligan, D. B. Doyle, K. J. Kinser, and M. Lockwood (1990), A statistical study of large field-aligned flows of thermal ions at high-latitudes, *Planet. Space Sci.*, *9*, 1187–1201.
Khazanov, G. V., M. W. Liemohn, and T. E. Moore (1997), Photoelectron effects on the self-consistent potential in the collisionless polar wind, *J. Geophys. Res.*, *102*(A4), 7509–7521.
Khazanov, G. V., M. W. Liemohn, E. N. Krivorutsky, and T. E. Moore (1998), Generalized kinetic description of a plasma in an arbitrary field-aligned potential energy structure, *J. Geophys. Res.*, *103*(A4), 6871–6889.
Khazanov, G. V., A. Glocer, and E. W. Himwich (2014), Magnetosphere-ionosphere energy interchange in the electron diffuse aurora, *J. Geophys. Res. Space Physics*, *119*, 171–184, doi:10.1002/2013JA019325.
Lorentzen, D., J. I. Moen, K. Oksavik, F. Sigernes, Y. Saito, and M. G. Johnsen (2010), In situ measurement of a newly created polar cap patch, *J. Geophys. Res.*, *115*, A12323, doi:10.1029/2010JA015710.
Lund, E. J., et al. (2012), Electron temperature in the cusp as measured with the SCIFER-2 sounding rocket, *J. Geophys. Res.*, *117*, A06326, doi:10.1029/2011JA017404.
Lynch, K. A., et al. (2014), MICA sounding rocket observations of conductivity-gradient-generated auroral ionospheric responses: Small-scale structure with large-scale drivers, *J. Geophys. Res. Space Physics*, doi:10.1002/2014JA020860.
Mechtly, E. A., S. A. Bowhill, and L. G. Smith (1972), Changes of lower ionosphere electron concentrations with solar activity, *J. Atmos. Terr. Phys.*, *34*, 1899–1907.
Moen, J. I., X. C. Qiu, H. C. Carlson, R. Fujii, and I. W. McCrea (2008), On the diurnal variability in F2-region plasma density above the EISCAT Svalbard radar, *Ann. Geophys.*, *26*, 2427–2433.
Ogawa, Y., R. Fujii, S. C. Buchert, S. Nozawa, and S.-I. Ohtani (2003), Simultaneous EISCAT Svalbard radar and DMSP observations of ion upflow in the dayside polar ionosphere, *J. Geophys. Res.*, *108*(A3), 1101, doi:10.1029/2002JA009590.
Ogawa, Y., et al. (2008), Coordinated EISCAT Svalbard radar and Reimei satellite observations of ion upflows and suprathermal ions, *J. Geophys. Res.*, *113*, A05306, doi:10.1029/2007JA012791.
Ogawa, Y., S. C. Buchert, A. Sakurai, S. Nozawa, and R. Fujii (2010), Solar activity dependence of ion upflow in the polar ionosphere observed with the European Incoherent Scatter (EISCAT) Tromsø UHF radar, *J. Geophys. Res.*, *115*, A07310, doi:10.1029/2009JA014766.
Ogawa, Y., S. C. Buchert, I. Haggstrom, M. T. Rietveld, R. Fujii, S. Nozawa, and H. Miyaoka (2011), On the statistical relation between ion upflow and naturally enhanced ion-acoustic lines observed with the EISCAT Svalbard radar, *J. Geophys. Res.*, *116*, A03313, doi:10.1029/2010JA015827.
Picone, J. M., A. E. Hedin, D. P. Drob, and A. C. Aikin (2002), NRLMSISE-00 empirical model of the atmosphere: Statistical comparisons and scientific issues, *J. Geophys. Res.*, *107*(A12), 1468, doi:10.1029/2002JA009430.
Robineau, A., P.-L. Blelly, and J. Fontanari (1996), Time-dependent models of the auroral ionosphere above EISCAT, *J. Atmos. Terr. Phys.*, *58*(1–4), 257–271.
Schunk, R. W., and J. J. Sojka (1997), Global ionosphere-polar wind system during changing magnetic activity, *J. Geophys. Res.*, *102*(A6), 11,625–11,651.
Shelley, E. G., R. G. Johnson, and R. D. Sharp (1972), Satellite observations of energetic heavy ions during a geomagnetic storm, *J. Geophys. Re.*, *77*(31), 6104–6110.
Skjæveland, Å., J. Moen, and H. C. Carlson (2014), Which cusp upflow events can possibly turn into outflows?, *J. Geophys. Res. Space Physics*, *119*, 6876–6890, doi:10.1002/2013JA019495.
Strangeway, R. J., R. E. Ergun, Y.-J. Su, C. W. Carlson, and R. C. Elphic (2005), Factors controlling ionospheric outflows as observed at intermediate altitudes, *J. Geophys. Res.*, *110*, A03221, doi:10.1029/2004JA010829.
Varney, R. H., W. E. Swartz, D. L. Hysell, and J. D. Huba (2012), SAMI2-PE: A model of the ionosphere including multistream interhemispheric photoelectron transport, *J. Geophys. Res.*, *117*, A06322, doi:10.1029/2011JA017280.
Varney, R. H., S. C. Solomon, and M. J. Nicolls (2014), Heating of the sunlit polar cap ionosphere by reflected photoelectrons, *J. Geophys. Res. Space Physics*, *119*, 8660–8684, doi:10.1002/2013JA019378.
Wahlund, J.-E., H. J. Opgenoorth, I. Haggstrom, K. J. Kinser, and G. O. L. Jones (1992), EISCAT observations of topside ionospheric ion outflows during auroral activity: Revisited, *J. Geophys. Res.*, *97*(A3), 3019–3037.
Wang, H., and H. Luhr (2013), Seasonal variation of the ion upflow in the topside ionosphere during SAPS (subauroral polarization stream) periods, *Ann. Geophys.*, *31*(9), 1521–1534.

Yau, A. W., P. H. Beckwith, W. K. Peterson, and E. G. Shelley (1985), Long-term (solar cycle) and seasonal variations of upflowing ionospheric ion events at DE 1 altitudes, *J. Geophys. Res.*, *90*(A7), 6395–6407.

Zettergren, M., K. A. Lynch, D. L. Hampton, M. J. Nicolls, B. Wright, M. G. Conde, J. I. Moen, M. R. Lessard, R. Miceli, and S. P. Powell (2014), Auroral ionospheric F region density cavity formation and evolution: MICA campaign results, *J. Geophys. Res. Space Physics*, *119*, 3162–3178, doi:10.1002/2013JA019583.

Zhang, B.-C., W. Lotko, O. J. Brambles, M. J. Wiltberger, W. Wang, P. Schmitt, and J. G. Lyon (2012), Enhancement of thermospheric mass density by soft electron precipitation, *Geophys. Res. Lett.*, *39*, L20102, doi:10.1029/2012GL053519.

Zhang, S.-R., and J. M. Holt (2004), Ionospheric plasma temperatures during 1976–2001 over Millstone Hill, *Adv. Space Res.*, *33*(6), 963–969.